Proceedings of the ASME 2023
International Mechanical Engineering Congress and Exposition
IMECE2023
October 29-November 2, 2022, New Orleans, Louisiana

IMECE2023-112572

HYDRODYNAMICS OF METACHRONAL ROWING AT INTERMEDIATE REYNOLDS NUMBERS

Menglong Lei
Department of Mechanical Engineering,
Villanova University
Villanova, PA

Zhipeng Lou
Department of Mechanical Engineering,
Villanova University
Villanova, PA

Junshi Wang
Department of Mechanical and Aerospace Engineering,
Princeton University,
Princeton, NJ

Haibo Dong
Department of Mechanical and Aerospace Engineering,
University of Virginia,
Charlottesville, VA

Chengyu Li
Department of Mechanical Engineering,
Villanova University
Villanova, PA

ABSTRACT

Metachronous rowing is a swimming mechanism widely adopted by small marine invertebrate like comb jellies, in which rows of appendages perform propulsive strokes sequentially in a coordinated manner with a fixed phase difference. To simulate metachronous rowing at intermediate Reynolds number, in this paper, a row of flexible cilia models was placed inside the flow field, with their roots stroke at a sinusoidal function of time and a fixed phase difference. A fully coupled two-way numerical solver was developed, which solves the Navier-Stokes equations for the fluid field coupled with the differential equation for the flexible cilia model. This numerical solver is applied to investigate how the row of cilia models are deformed by the hydrodynamic forces (pressure and shear) and momentum and thus impact hydrodynamic performance. Results show that the passive deformation of cilia potentially improve the hydrodynamic performance compared to the rigid cilia. With the metachronous rowing mechanism, the cilia generate the thrust to move forward. The approach used in this study presents a general way to explore the fluid dynamics of complex fluid-structure interaction problems.

Keywords: Fluid Structure Interaction (FSI), cilia, Finite Element Method (FEM), Computational Fluid Dynamics (CFD)

1. INTRODUCTION

Small swimming invertebrates like comb jellies are able to move efficiently through fluids using metachronous rowing [1], a movement mechanism where rows of appendages perform propulsive strokes sequentially in a coordinated manner with a fixed phase difference from their neighboring appendages [2]. This metachronous stroke pattern potentially benefits the efficiency of the propulsion in fluids [3]. The cilia propulsion mechanism is relatively simple compared to other propelling mechanisms in fish and swimming mammals. However, we have limited understanding on how the cilia motion is controlled by comb jellies. As the cilia strokes back and force, asymmetric motion between the power stroke and recovery stroke of the cilia is observed and attributed to the thrust generation. It is possible that the asymmetric motion arises from the mixed effects of the asymmetric active muscle control at the root of the cilia and the hydrodynamic forces on the cilia.

To address this question, research has been conducted to study hydrodynamics of flexible cilia-like material. Early studies simulated cilia metachronous motion without solving the Navier-Stokes equations for the fluid field [4-7] thus cannot obtain the hydrodynamic force on the cilia. Experiments, on the other hand, were adopted to measuring velocity field in ciliary propulsion problems [2, 3]. Later studies were able to numerically simulate cilia motion using Fluid Structure Interaction (FSI). Dai et al. [8] solved the hydrodynamics of a flexible pitching plate. Liu et al.

[9], Luo et al. [10], and Wang et al. [11] used FSI to solve fish tail shaped materials. Their studies demonstrated the potentiality of using FSI to solve passive deformation problems. However, these numerical studies were limited to single deformable body thus cannot include the interaction between multiple bodies.

In this study, numerical simulations of ctenophores (comb jellies) swimming were performed to investigate the hydrodynamic mechanisms of the metachronous rowing motion of cilia. We aim to understand the effects of cilia motion in the hydrodynamics performance. The metachronous motion of the cilia was achieved by simulating the oscillations of a row of flexible cilia that are hinge-linked to a wall inside fluids, with the motion of root of the cilia being prescribed and the motion of other parts being calculated by Fluid Structure Interaction between the cilia and fluid. An in-house immersed-boundary-method based Computational Fluid Dynamics (CFD) solver was used to solve the Navier-Stokes equations for the flow filed. A Finite Element Method (FEM) solid solver Vega FEM was then used to solve the deformation of the cilia subjected to the pressure and shear on the cilia. We aim to study the fundamental mechanism of the hydrodynamics of the cilia metachronous rowing motion and bring more insights to the designing of bio-inspired miniaturized swimming robots in the low-to-intermediate Reynolds number regime.

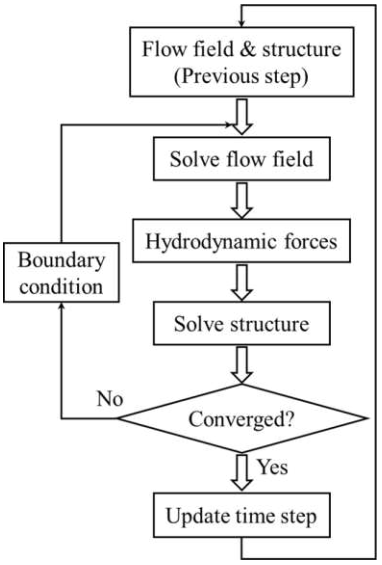

FIGURE 1. OUTLINE OF THE PROCESSES IN SOLVING THE FLUID-STRUCTURE INTERACTION PROBLEM.

2. MATERIALS AND METHODS

2.1 Overview of the coupled Fluid Structure Interaction solver

The current study employs an in-house CFD solver and a FEM structure solver (Vega FEM). The two solvers are strongly coupled to solve the Fluid Structure Interaction problems. Figure 1 shows the flow chart in solving the fluid-structure interaction problems. To couple the CFD solver and structure solver together, a convergence state must be achieved so that the hydrodynamic forces on the structure balance the internal forces inside the structure and the momentum forces.

2.2 Flow field solver

The flow filed is governed by the incompressible Navier-Stokes equations. The equations are written in tensor form:

$$\begin{cases} \dfrac{\partial u_i}{\partial x_i} = 0 \\ \dfrac{\partial u_i}{\partial t} + \dfrac{\partial \left(u_i u_j\right)}{\partial x_j} = -\dfrac{1}{\rho}\dfrac{\partial P}{\partial x_i} + \nu \dfrac{\partial}{\partial x_j}\left(\dfrac{\partial u_i}{\partial x_j}\right) \end{cases} \tag{1}$$

Where u_i are the velocity component, P is the pressure, ρ is the fluid density, ν is the kinematic viscosity.

The above equations are discretized using a cell-centered, collocated arrangement of the primitive variables, and are solved using a finite difference-based immersed-boundary method [12] in a non-body-conforming Cartesian grid. A second-order central difference scheme is employed in space to discretize the advection and diffusion term. This CFD solver has been successfully applied to study canonical revolving wings [13-16], flapping propulsion problems [17-23], passive wing pitch mechanism [24-27],and insect flight [28-35].

2.3 Finite Element Method structure solver

To solve the dynamics of the solid structure, the Vega FEM open-source code [36] was used, which takes the hydrodynamic forces (pressure and shear) on the solid calculated from the fluid field as the input, and calculate the deformations of solid structure. The Vega FEM code solves the following solid dynamics equation using finite element method:

$$M\ddot{X}_b + D\dot{X}_b + f_{int}\left(X_b\right) = f_{ext} \tag{2}$$

Where X_b is the displacement of the mesh vertices of the solid, M is the mass matrix, D is the damping matrix, f_{int} is the internal elastic forces, f_{ext} is the external hydrodynamic forces on the vertices. The St. Venant-Kirchhoff nonlinear material model was employed for the structure solver, defined by the energy density function as:

$$\Psi = \mu \mathbf{E} : \mathbf{E} + \frac{\lambda}{2} tr^2\left(\mathbf{E}\right) \tag{3}$$

Where λ and μ are the Lamé coefficients, $\mathbf{E}$ is the Green strain tensor.

2.4 Hydrodynamic Performance

The kinematics of the cilia models and flow field conditions are presented in Figure 2. The stroke angles of the cilia models are prescribed by Eq. 4. While the passive deformation is calculated from Fluid-Structure Interaction.

$$\theta = \theta_0 \sin\left(2\pi f t + \varphi\right) \tag{4}$$

Where θ_0 is the stroke magnitude, φ are the phase differences of the cilia models. For the five cilia models, φ are 0, $\pi/4$, $\pi/2$, $3\pi/4$, and π, respectively. The cilia model consisting of unstructured grids is shown in Figure 3.

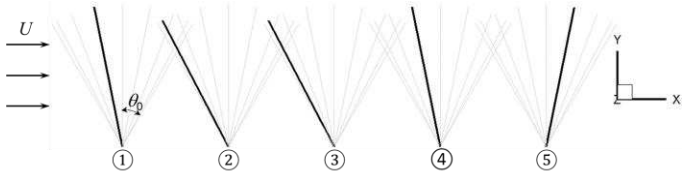

FIGURE 2. PRESCRIBED STROKE ANGLES AT THE ROOT OF A ROW OF CILIA MODELS. SOLID BLACK LINES DENOTE THE CILIA MODELS AT T/T = 0.0625.

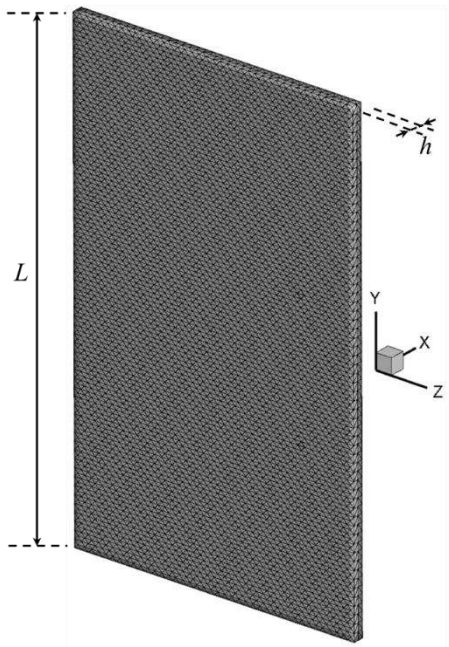

FIGURE 3. CILIA MODEL FOR THE FSI CALCULATION.

In this study, the Reynolds number $\mathrm{Re}_\omega = 52.92$, the reduced stiffness $K = 4.39$, mass ratio $M = 0.375$, which are defined as:

$$\mathrm{Re}_\omega = \frac{2\pi f L^2}{\nu}, \quad K = \frac{EI}{\rho_s U^2 L^3}, \quad M = \frac{\rho_s h}{\rho_f L} \tag{5}$$

Where U is the incoming flow velocity, L is the length of the cilia model, ν is the kinematic viscosity of the fluid, E is the Young's modulus of the cilia model, ρ_s is the density of the cilia model, h is the thickness of the cilia model, $I = h^3/12$ is the area momentum of inertia of the cross section.

2.5 Grid Independence Study

To ensure the simulation results are grid-independent, a grid-independence study was conducted. Simulations of the same cilia metachronal rowing motion were performed in three different grids, coarse grid, current grid, and fine grid. The time history of drag coefficients for the three grids are shown in Figure 4. The results for the three grids are generally the same. We see the results for the current grid are nearly identical to the results of the fine grid, which indicates the simulation in the current study is grid independent.

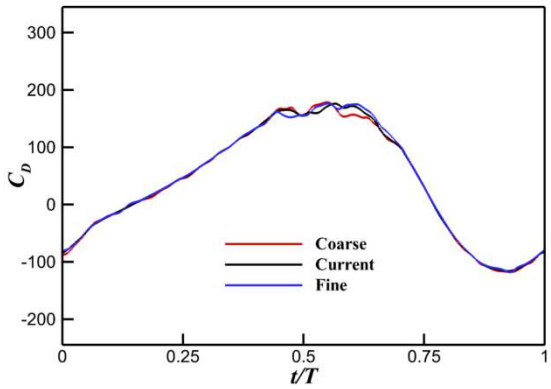

FIGURE 4. COMPARISON OF DRAG COEFFICIENTS USING COARSE GRID (256 × 96 = 2.4 × 10^4), CURRENT GRID (288 × 128 = 3.8 × 10^4), AND FINE GRID (320 × 160 = 5.1 × 10^4).

3. RESULTS

Figure 5 shows the time history of drag coefficient $C_D = 2F_x/\left(\rho_f U^2 S\right)$ during a stroke cycle, where F_x is the hydrodynamic force on the cilia modes, S is the area of the cilia model. We see a phase difference in the drag coefficients which correspond to the phase difference of the prescribed stroke motion in the setup. The cycle-averaged drag coefficients for the 5 cilia models are 41.6, -18.1, -13.4, 4.1, and -22.3, respectively. The overall drag coefficient for the metachronal rowing motion of the 5 cilia models is -8.1, which is thrust. Since the stroke motion for all the cilia models are symmetric during up- and downstroke, it is reasonable to observe positive drag coefficients. However, thrust is generated by metachronal rowing motion. We see cilia 1 generates most of the drag and cilia 5 generates most of the thrust. Note that cilia 1 is at the upstream location and cilia 5 is at the downstream location. The thrust generation is related to the position of the cilia models and the phase difference of stroke motion.

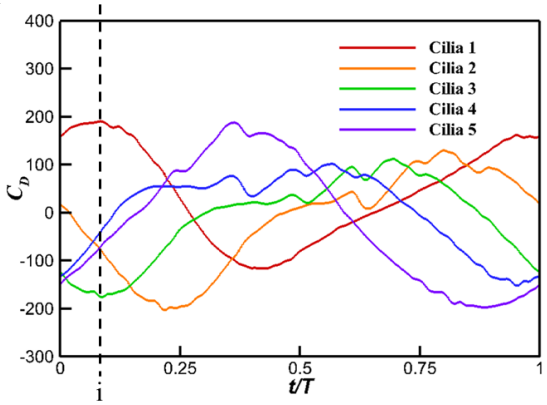

FIGURE 5. TIME HISTORY OF THE DRAG COEFFICIENTS FOR THE 5 CILIA MODELS. NEGATIVE DRAG DENOTES THRUST. THE BLACK DASHED LINE DENOTES THE TIME AT T/T = 0.083, AT WHICH THE DRAG IS MAXIMIZED ON CILIA 1 AND MINIMIZED ON CILIA 3.

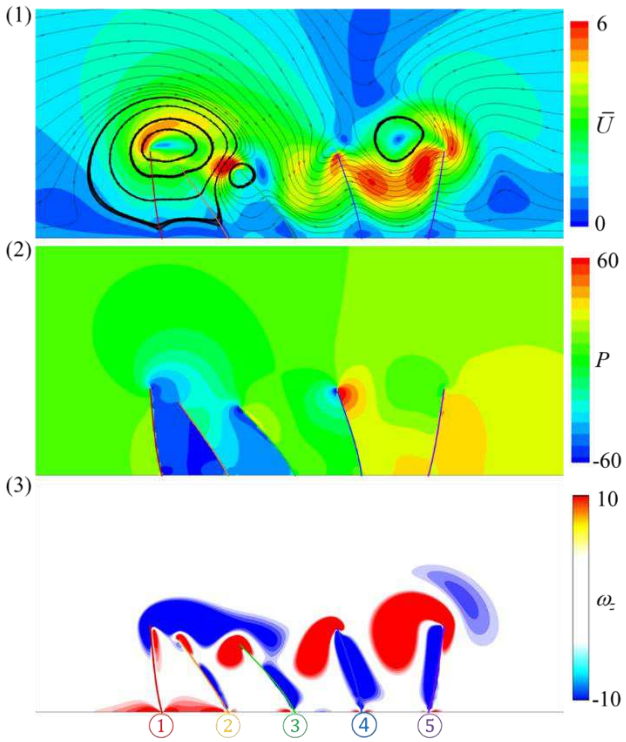

FIGURE 6. VELOCITY MAGNITUDE CONTOUR PLOTTED WITH STREAMLINES (1), PRESSURE CONTOUR (2), VORTICITY IN THE Z-DIRECTION (ω_Z) (3) AT T/T = 0.083. THE COLOR OF THE CILIA MODELS CORRESPONDS TO THE COLOR OF DRAG COEFFICIENT IN FIGURE 5.

The time instant i at t/T = 0.083 is highlighted in Figure 5**,** at which the drag is maximized on cilia 1 and minimized on cilia 3. To explain this observation, we plotted the velocity magnitude contour with streamlines, pressure contour, vorticity in the z-direction (ω_z) at t/T = 0.083 in Figure 6. Cilia 1 is sweeping left, which creates a huge pressure difference between the left and right sides, leading to large drag generation. Cilia 3, 4, and 5 are sweeping right, thus generating thrust. However, cilia 2 is sweeping left but generating thrust. The possible reason is the lager area of low-pressure region observed between cilia 1 and cilia 2.

4. CONCLUSION

In this study, a fully coupled two-way numerical solver was developed, which solves the Navier-Stokes equations for the fluid field coupled with the differential equation for the flexible cilia model. Iterations between the two solvers ensure that the hydrodynamic forces acted on the structure balance the internal forces inside the structure and the momentum forces. Our calculation results show that the row of cilia models is deformed by the hydrodynamic forces. Interactions between the cilia models greatly impact the hydrodynamic performance of different cilia models at different locations. Thrust generation was observed even with symmetric stroke kinematics of the cilia model.

Since the stroke kinematics for each cilia model is symmetric, the reason of the thrust generation lies in the metachronous rowing motion, in which the cilia models stroke sequentially with a fixed phase difference. With an increasing phase difference of the cilia in the flow direction, the asymmetric metachronous rowing motion thus generates thrust.

Our calculations demonstrated the potentiality of using FSI to solve passive deformation problems.

ACKNOWLEDGEMENTS

This research was supported by the National Science Foundation (NSF CBET-2120505) to C. Li. All simulations were run on the High-Performance Computing Cluster of the College of Engineering at Villanova University.

REFERENCES

[1] Matsumoto, G., 1991, "Swimming movements of ctenophores, and the mechanics of propulsion by ctene rows," Hydrobiologia, 216, pp. 319-325.
[2] Barlow, D., and Sleigh, M. A., 1993, "Water propulsion speeds and power output by comb plates of the ctenophore Pleurobrachia pileus under different conditions," Journal of experimental biology, 183(1), pp. 149-164.
[3] Barlow, D., Sleigh, M. A., and White, R. J., 1993, "Water flows around the comb plates of the ctenophore Pleurobrachia plotted by computer: a model system for studying propulsion by antiplectic metachronism," Journal of experimental biology, 177(1), pp. 113-128.
[4] Blake, J., 1971, "Infinite models for ciliary propulsion," Journal of Fluid Mechanics, 49(2), pp. 209-222.
[5] Brennen, C., 1974, "An oscillating-boundary-layer theory for ciliary propulsion," Journal of Fluid Mechanics, 65(4), pp. 799-824.
[6] Blake, J. R., 1971, "A spherical envelope approach to ciliary propulsion," Journal of Fluid Mechanics, 46(1), pp. 199-208.
[7] Lou, Z., Herrera-Amaya, A., Byron, M. L., and Li, C., "Hydrodynamics of Metachronal Motion: Effects of Spatial Asymmetry on the Flow Interaction Between Adjacent Appendages," Proc. Fluids Engineering Division Summer Meeting, American Society of Mechanical Engineers, 2022, Vol. 85840, p. V002T005A016.
[8] Dai, H., Luo, H., de Sousa, P. J. F., and Doyle, J. F., 2012, "Thrust performance of a flexible low-aspect-ratio pitching plate," Physics of Fluids, 24(10), p. 101903.
[9] Liu, G., Geng, B., Zheng, X., Xue, Q., Dong, H., and Lauder, G. V., 2019, "An image-guided computational approach to inversely determine in vivo material properties and model flow-structure interactions of fish fins," Journal of Computational Physics, 392, pp. 578-593.
[10] Luo, Y., Xiao, Q., Shi, G., Pan, G., and Chen, D., 2020, "The effect of variable stiffness of tuna-like fish body and fin on swimming performance," Bioinspiration & biomimetics, 16(1), p. 016003.
[11] Wang, J., Lauder, G., and Dong, H., "Effect of tunable stiffness on the hydrodynamic performance of a tuna tail

informed flexible propulsor," Proc. AIAA SCITECH 2022 Forum, p. 0729.
[12] Wan, H., Dong, H., and Huang, G. P., 2012, "Hovering hinge-connected flapping plate with passive deflection," AIAA journal, 50(9), pp. 2020-2027.
[13] Li, C., Dong, H., and Cheng, B., 2017, "Effects of aspect ratio and angle of attack on tip vortex structures and aerodynamic performance for rotating flat plates," AIAA 2017-3645, p. 3645.
[14] Wan, H., Dong, H., Li, C., and Liang, Z., 2012, "Vortex Formation and Aerodynamic Force of Low Aspect-Ratio Plate in Translation and Rotation," AIAA Paper 2012-3278.
[15] Li, C., Dong, H., and Cheng, B., 2020, "Tip vortices formation and evolution of rotating wings at low Reynolds numbers," Physics of Fluids, 32(2), p. 021905.
[16] Wang, J., Li, C., Zhu, R., Liu, G., and Dong, H., 2019, "Wake structure and aerodynamic performance of passively pitching revolving plates," AIAA paper 2019-1376.
[17] Li, C., and Dong, H., 2016, "Three-dimensional wake topology and propulsive performance of low-aspect-ratio pitching-rolling plates," Phys. Fluids, 28(7), p. 071901.
[18] Li, C., Dong, H., and Liu, G., 2015, "Effects of a dynamic trailing-edge flap on the aerodynamic performance and flow structures in hovering flight," J. Fluid Struct., 58, pp. 49-65.
[19] Wang, J., Li, C., Ren, Y., and Dong, H., 2017, "Effects of surface morphing on the wake structure and performance of flapping plates," AIAA paper 2017-3643.
[20] Li, C., and Dong, H., 2016, "Quantification and Analysis of Propulsive Wake Topologies in Finite Aspect-Ratio Pitching-Rolling Plates," AIAA Paper 2016-4339.
[21] Xu, M., Wei, M., Li, C., and Dong, H., 2019, "Adjoint-based optimization for thrust performance of three-dimensional pitching–rolling plate," AIAA Journal, 57(9), pp. 3716-3727.
[22] Menzer, A., Li, C., Fish, F., Gong, Y., and Dong, H., "Modeling and Computation of Batoid Swimming Inspired Pitching Impact on Wake Structure and Hydrodynamic Performance," Proc. Fluids Engineering Division Summer Meeting, American Society of Mechanical Engineers, 2022, Vol. 85840, p. V002T005A003.
[23] Lei, M., Crimaldi, J. P., and Li, C., "Navigation in odor plumes: How do the flapping kinematics modulate the odor landscape?," Proc. AIAA AVIATION 2021 FORUM, p. 2817.
[24] Li, C., Wang, J., Liu, G., Deng, X., and Dong, H., "Passive pitching mechanism of three-dimensional flapping wings in hovering flight," Proc. Fluids Engineering Division Summer Meeting, American Society of Mechanical Engineers, 2019, Vol. 59032, p. V002T002A043.
[25] Lei, M., and Li, C., 2020, "The aerodynamic performance of passive wing pitch in hovering flight," Physics of Fluids, 32(5), p. 051902.
[26] Lei, M., and Li, C., "Numerical investigation of the passive pitching mechanism in odor-tracking flights," Proc. AIAA AVIATION 2020 FORUM, p. 3016.
[27] Lei, M., and Li, C., "Effects of Wing Kinematics on Modulating Odor Plume Structures in the Odor Tracking Flight of Fruit Flies," Proc. Fluids Engineering Division Summer Meeting, American Society of Mechanical Engineers, 2021, Vol. 85284, p. V001T002A022.
[28] Li, C., and Dong, H., 2017, "Wing kinematics measurement and aerodynamics of a dragonfly in turning flight," Bioinspir. Biomim., 12(2), p. 026001.
[29] Li, C., Dong, H., and Zhao, K., 2020, "Dual functions of insect wings in an odor-guided aeronautic navigation," Journal of fluids engineering, 142(3), p. 030902.
[30] Dong, H., Bode-Oke, A. T., and Li, C., 2018, Learning from nature: unsteady flow physics in bioinspired flapping flight, InTech.
[31] Li, C., Dong, H., and Zhao, K., 2018, "A balance between aerodynamic and olfactory performance during flight in Drosophila," Nature communications, 9(1), pp. 1-8.
[32] Li, C., 2021, "Effects of wing pitch kinematics on both aerodynamic and olfactory functions in an upwind surge," Proceedings of the Institution of Mechanical Engineers, Part C: Journal of Mechanical Engineering Science, 235(2), pp. 296-307.
[33] Liu, Y., Lozano, A. D., Hedrick, T. L., and Li, C., 2021, "Comparison of experimental and numerical studies on the flow structures of hovering hawkmoths," Journal of Fluids and Structures, 107, p. 103405.
[34] Lionetti, S., Hedrick, T. L., and Li, C., 2022, "Aerodynamic explanation of flight speed limits in hawkmoth-like flapping-wing insects," Physical Review Fluids, 7(9), p. 093104.
[35] Lei, M., and Li, C., "A Balance Between Odor Intensity and Odor Perception Range in Odor-Guided Flapping Flight," Proc. Fluids Engineering Division Summer Meeting, American Society of Mechanical Engineers, 2022, Vol. 85840, p. V002T005A002.
[36] Sin, F. S., Schroeder, D., and Barbič, J., "Vega: non-linear FEM deformable object simulator," Proc. Computer Graphics Forum, Wiley Online Library, 2013, pp. 36-48.